Chapter 4
Monolithic Silicon Photonic Crystal Fiber Tip Sensors

Bryan Park and Olav Solgaard

Abstract Photonic Crystals (PC) enable sensitive and robust sensors for a large number of measurands, including temperature, refractive index, displacement, pressure, acceleration, and rotation. The small volumes of two-dimensional PC sensors also make them ideal for integration onto the facet of optical fibers. In this chapter, we describe the operation, design, and fabrication of Si PC sensors for refractive index and temperature, and the process technology used to integrate the sensors onto the facets of standard single-mode fibers (SMFs). The PC sensors are fabricated on standard Si wafers, using a single photolithography mask and a combination of isotropic and anisotropic etching. Once the sensor fabrication is completed, the miniaturized sensors (50 μm × 50 μm × 0.5 μm) are assembled onto SMF facets. The results are highly-sensitive, robust sensors with submicron sensing layers that are well suited for deployment in harsh environments, including temperatures up to 700 °C.

4.1 Introduction

Fiber optic sensors have been intensively developed and deployed in a wide variety of applications due to their unique advantages: small size, high sensitivity, insusceptibility to electromagnetic interference, chemical and mechanical robustness, wavelength multiplexing, and distributed sensing capabilities. They have been used to measure various physical quantities such as refractive index, temperature, strain,

B. Park · O. Solgaard (✉)
E. L. Ginzton Laboratory, Department of Electrical Engineering,
Stanford University, Stanford, CA 94305, USA
e-mail: solgaard@stanford.edu

B. Park
e-mail: insun@stanford.edu

A. Cusano et al. (eds.), *Lab-on-Fiber Technology*,
Springer Series in Surface Sciences 56, DOI: 10.1007/978-3-319-06998-2_4,

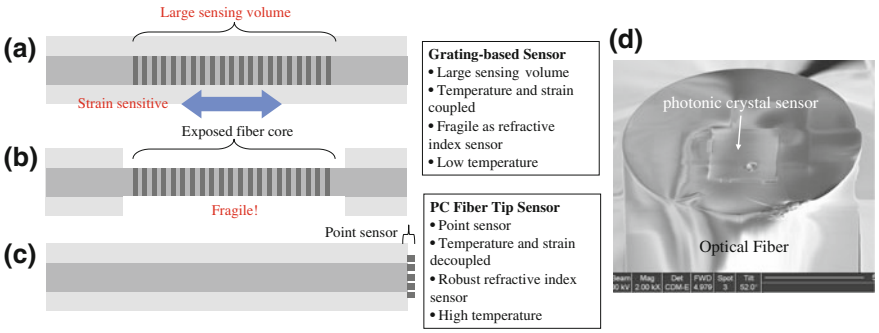

Fig. 4.1 **a** Grating-based fiber sensors require large sensing volumes and are subject to undesired strain sensitivity. **b** core-exposed FBG refractive index sensors for higher sensitivity become fragile. **c** compact and robust PC fiber tip sensors are insensitive to external strain. **d** SEM image of a PC fiber tip sensor. A silicon PC sensor covers the core of the fiber and interacts with the surrounding environment

pressure, and acceleration with different detection methods [1, 2]. They are especially promising for use under harsh conditions, e.g. high temperatures, corrosive, noisy, and high-voltage environments, because their structural materials, typically glasses, can withstand high temperatures, above 500 °C, while conventional electronics fail to operate at such temperatures due to the intrinsic properties of semiconductors and metal contacts/interconnects. Most commonly used fiber sensors are grating-based fiber sensors (Fig. 4.1a), which include fiber Bragg grating (FBG) and long-period fiber gratings (LPFG). In FBG sensors, the silica fiber core is photo-inscribed with a periodic refractive index contrast along the light propagation direction through ultraviolet exposure [3, 4], and the grating structure functions as spectral filter whose characteristics alter according to changes in the surrounding environment. LPFG sensors have long-period gratings ($\sim$100 μm) and couple the fundamental mode into forward-propagating cladding modes that interact with materials outside the cladding and therefore detect changes in ambient conditions [5]. Although grating-based sensors have many advantages compared to other sensors, they also suffer from significant drawbacks. Many periods are needed for grating functionality, and, accordingly, these sensors have large sensing volumes and are vulnerable to unwanted coupling to external strains. In order for FBGs to have better refractive index sensitivity, their fiber cores are directly exposed to the environment by removing their claddings, but this process compromises their structural strength and durability (Fig. 4.1b) [6]. They also have low sensitivity to temperature ($\sim$0.01 nm/°C), and require isolators to prevent back reflections into the laser, which poses significant difficulties in practical system implementation. The LPFG have higher temperature sensitivity ($\sim$0.1 nm/°C) and low back reflections, but their sensing lengths are even longer ($\sim$a few centimeters) due to their long periodicities [7]. In addition, both types have a fundamental problem in high temperature applications; at temperatures above 200 °C, UV-written gratings are erased [8]. FBG sensors with direct etching of gratings in their fiber cores have

been demonstrated [9], but this approach complicates the fabrication process and inevitably reduces the mechanical strength of the sensors.

In this chapter, we introduce a hybrid structure where a very compact two-dimensional silicon photonic crystal (PC) is attached on a tip of a single mode optical fiber (Fig. 4.1c, d) in order to overcome the problems of fiber-only sensors (i.e. limited sensitivity, large sensing length, fragile structure) [10, 11]. The small PC membrane (50 μm × 50 μm × 0.5 μm) is completely confined to the fiber facet and it has high sensitivity to changes in refractive index and temperature. The resulting device is a small and robust reflection-based sensor that interacts with the measurand in a small volume, approaching a point sensor at the tip of the fiber. Other hybrid fiber sensors based on plasmonic-resonances of gold nanoparticles also have been demonstrated [12], but the use of the low-temperature metal limits its range of applications because the metal may melt or degrade in corrosive, high temperature, high optical power environments. In contrast, our sensor is made of chemically-robust high temperature dielectric materials, silicon and glass, and is therefore well-suited for operation in harsh environments. The PC-on-fiber configuration is flexible and can be employed in a variety of applications, including inertial sensors and hydrophones [13].

In Sect. 4.2, we introduce the working principle of PC sensors based on the guided resonance phenomenon. Then we describe the fabrication of the PC and the assembly of the PC on the fiber tip in the Sect. 4.3. Section 4.4 includes the experimental characterization of the PC fiber tip sensor, showing high sensitivity to refractive index and temperature. High temperature measurement up to 900 °C is also presented in this section. Lastly, we conclude the chapter in Sect. 4.5.

4.2 Photonic Crystals Fundamentals

PCs are optical nanostructures with subwavelength periodic modulation of the dielectric constants. They provide means to control and manipulate photons in similar ways to how semiconductors control electrons. PCs have photonic band structures determined by their constituent materials and crystal organization, and the presence or absence of modes at a range of wave vectors and wavelengths lead to many interesting and useful phenomena, such as photonic bandgaps, superprism effects, negative refraction, and guided resonances [14–17], allowing them to be used in a variety of applications including waveguides, high-Q cavities, sensors, and mirrors [18–21].

PCs can be fabricated in one, two, or three-dimensional structures. The most well-known one-dimensional (1-D) PCs are Bragg reflectors, in which periodic layers of alternating high and low refractive index are cascaded to form high-quality mirrors (Fig. 4.2a). The Bragg reflectors are particularly useful at optical frequencies where metal mirrors suffer from significant absorption loss, finding their applications in vertical-external-cavity surface-emitting-lasers (VECSELs)

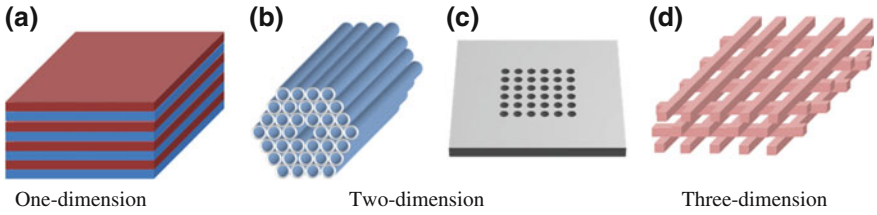

Fig. 4.2 Photonic crystals. **a** One-dimensional Bragg reflector. **b** Two-dimensional PC holey fiber. **c** Two-dimensional PC slab. **d** Three-dimensional woodpile structure

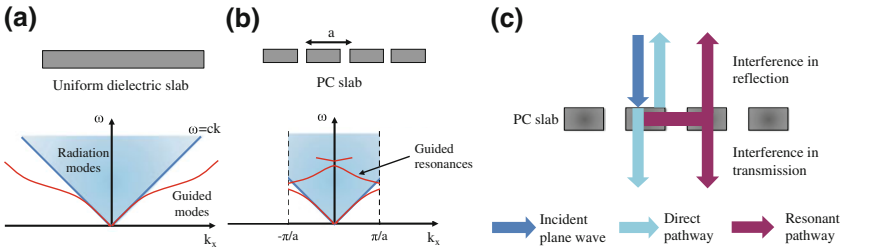

Fig. 4.3 Physical origin of guided resonances in 2-D PC slabs: **a** Band structure for a uniform dielectric slab. **b** Band structure for a 1-D PC slab. In the PC slab, the originally guided modes can couple to radiation modes due to phase matching provided by the periodic holes, resulting in guided resonances with finite lifetimes [28]. **c** Transmission and reflection of the 2-D PC are determined by interference between the direct pathway and resonant pathways arising from coupling to guided resonances

and optical MEMS systems. Two-dimensional (2-D) PCs come in two different versions; fibers and patterned thin films as shown in Fig. 4.2b and c. PC fibers are patterned so that photons at target wavelengths are confined to the core by an in-plane bandgap. For example, holey fibers support one or more guided modes at their center void because surrounding hexagonally periodic structures provide a photonic bandgap (Fig. 4.2b) [22]. The defining example of a thin-film PC is a 2-D PC slab where periodic patterns, typically square or hexagonal lattices, are etched into a thin film of high refractive index surrounded by low refractive index materials (Fig. 4.2c). Such 2-D PC slabs have been employed in many photonic devices because their optical properties, e.g. transmission and reflection, can be designed to support a wide range of applications from highly sensitive sensors to broadband reflectors. Furthermore, their fabrication is relatively straightforward, and their compact size and planar geometry facilitate integration with ICs and MEMS [23]. Three-dimensional (3-D) PCs (e.g. the woodpile structure in Fig. 4.2d) with a complete bandgap offer the ultimate control of photons [24, 25], but their fabrication has proven challenging up to this point although novel methods, such as direct laser writing and self-assembly of nanospheres, have been devised [26, 27].

In this chapter, we focus on a 2-D PC slab with a square lattice of cylindrical air holes in a thin silicon membrane. Our 2-D PC slab-integrated fiber sensors rely on guided resonances of the PCs [17]. In order to understand the physics of the guided resonances, we consider a 1-D PC slab with periodic air holes only in one lateral direction for simplicity. In a uniform dielectric slab without holes (Fig. 4.3a), the band diagram is divided into two regions by the light line, which is defined as $\omega = ck$ where ω is the angular frequency, c is the speed of light in vacuum, and k is the wave vector. A continuum of radiation modes, which can propagate in the surrounding medium, exists above the light line. Modes below the light line are "guided modes" whose electromagnetic field decays exponentially away from the dielectric slab. Therefore, their electromagnetic energies are completely confined to the slab and external radiation cannot couple to these guided modes. However, in the PC slab, scattering from the periodic hole arrays causes the dispersion relation of the guided modes to fold at the first Brillouin zone boundaries, and accordingly, some of the guided modes lie above the light line (Fig. 4.3b). This allows them to have radiative characteristics with finite lifetime. Theses modes, called guided resonances, are still confined within the slab, but can be excited from or couple to plane waves outside the PC slab.

The presence of the guided resonances brings about significant changes in the transmission and reflection of the PC slabs compared to the uniform dielectric slab. Assume a plane wave is normally incident on the PC. As in the uniform dielectric slab, some of the light are reflected back from the PC surfaces or directly propagates through the membrane. This forms the direct pathway through the PC. On the other hand, the incident light can excite guided resonances, and then the coupled light is radiated back to outside the PC with a characteristic lifetime. These resonant pathways interfere with the direct pathway as illustrated in Fig. 4.3c and determine the PC reflection and transmission spectra [29–32]. For example, if the interference is destructive on the transmission side and constructive on the reflection side over a wavelength band of interest, the PC slab can achieve high reflectivity near unity. Such spectral characteristics of the PC are closely related to the physical parameters of the PC: the lattice constant, the slab thickness, and the hole radius. The lattice constant decides the target operation range of the PC. If the material constants do not vary with wavelength, then the physical dimensions scale linearly in wavelength, but material dispersion is significant, so linear scaling is only approximately correct. For instance, lattice constants of 400 nm and 820 nm have been reported for PCs designed for visible and 1550 nm wavelengths respectively [21, 30]. The slab thickness and the hole diameter mainly determine the properties of the guided resonances. In general, larger holes and thinner slabs increase scattering and thereby decrease the lifetimes of the guided resonances. This effect results in broader resonances in the PC spectrum, which is desired in broadband, high-reflectivity mirrors. In contrast, smaller holes and thicker slabs have the opposite effect, leading to longer lifetimes, which yields sharper resonance features. The resonant peaks or dips shift in response to changes in surrounding environment and these shifts are particularly straightforward to

detect if the spectra contain sharp features, so long life time guided resonances are well suited to sensing applications.

Due to their compactness and mechanical robustness, 2-D PC mirrors have been incorporated into different platforms for beam steering [21, 23], polarization control [33], optical filtering [34], and sensing. PC sensors can be divided into two groups; Fabry-Perot-based sensors and spectral-shift sensors. In Fabry-Perot based PC sensors one of the mirrors of a Fabry-Perot resonator is a 2-D PC slab reflector. In these devices, broad band response of the PCs is preferable to make the sensors operable over wide range of laser wavelengths. Such sensors have been developed for measurements of acoustic waves [13, 35] and quasi-static pressure [36]. PC Fabry-Perot sensors can also be extended to incorporate near-field coupling, i.e. photon tunneling, effects [37] for added functionality.

Single-layer 2-D PC sensors based on spectral shifts of the PC reflection or transmission spectra also have received a lot of attention due to their potential as compact optical devices that measure a large variety of physical quantities, e.g. refractive index, and bio-molecule associations [38–40]. Their sensitivity to the surrounding media stems from the fact that the guided resonances in the PCs have evanescently decaying fields outside the PC slabs, and these evanescent fields interact with the media and these interactions determine the sensors, characteristics. The shifts or changes of the resonant features in response to changes in the media surrounding the PCs are monitored and analyzed for quantitative description on the measurand. We will explain the fabrication of the PC fiber tip sensors and their performance as sensors for refractive index and temperature in the Sect. 4.3.

4.3 Photonic Crystal Fabrication and Fiber Sensor Assembly

We fabricate the PC fiber tips sensors in two stages: fabrication of 2-D PCs on standard wafers in a silicon foundry and transfer of the PCs onto the facets of single-mode optical fibers.

4.3.1 Photonic Crystal Fabrication

We fabricate 2-D PC membranes on silicon wafers using the Generation of Photonic Elements by RIE (GOPHER) process, which employs a combination of anisotropic and isotropic etch steps together with thermal oxidation [41].

The process starts with thermal oxidation of silicon wafers to grow an oxide hard mask. Next we use a 5x reduction ASM-L i-line stepper to photolithographically inscribe the periodic arrays of cylindrical holes in photoresists spun on the wafers (Fig. 4.4a). A square lattice of circular holes is used as the PC pattern.

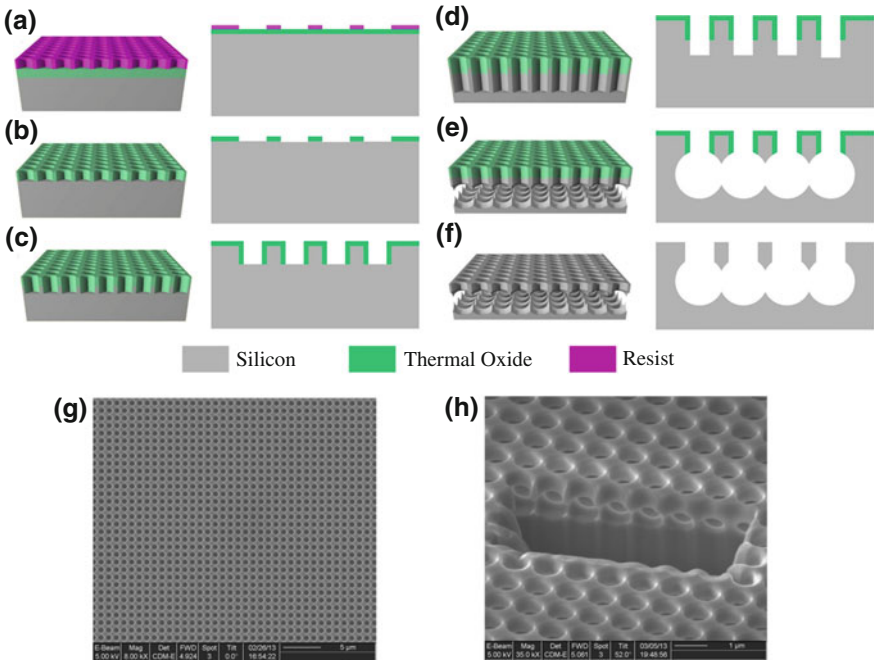

Fig. 4.4 2-D PC fabrication process flow: **a** Thermal oxidation and photolithography of the PC pattern. **b** Oxide layer etch by RIE to transfer the PC pattern from the resist into the oxide hard mask. **c** Si RIE, followed by conformal oxidation, and removal of oxide from the bottoms of the PC holes by RIE. **d** Hole extension into Si by RIE. **e** Isotropic Si etch for PC membrane release. **f** Oxide removal by HF. **g** *Top SEM view* of the fabricated PC. **h** *Crosssectional SEM* image of the PC with a section removed by a focused ion beam to reveal the structure of the PC

The optical stepper enables large-area patterns (e.g. 500 μm by 500 μm) with submicron-features to be patterned on entire wafers very quickly and also enables tuning of the PC optical characteristics by varying the hole size with different exposure doses given a single photomask [21]. Next, we transfer the PC pattern to the oxide hard mask (Fig. 4.4b) and subsequently to the silicon substrate by Reactive Ion Etching (RIE). The etched depth in the silicon layer determines the PC membrane thickness. Then, the exposed Si on the sidewalls and bottoms of the holes are covered with thin, conformal thermal silicon oxide. We perform a series of RIEs to remove the bottom oxide inside the holes without removing the sidewall oxide (Fig. 4.4c) and extend the holes into the silicon substrate (Fig. 4.4d). The side wall protection together with the hole extension beyond the sidewall protection determines the PC thickness after the upcoming isotropic silicon etching. The PC layer is then partially or completely released in a timed isotropic undercut etch. For fiber sensor applications, in which the PC is transferred onto an optical fiber facet, the undercut etch is performed until the PC membrane is completely released from the substrate (Fig. 4.4e). Finally, the oxide layer is removed by

vapor HF to minimize stress during release and avoid membrane stiction problems, which can arise from wet oxide etch (Fig. 4.4f). SEM pictures of a GOPHER-PC (periodicity = 1 μm, hole diameter = 700 nm, thickness = 650 nm) are shown as examples in Fig. 4.4g and h.

The GOPHER process has unique advantages compared to other PC fabrication technologies based on silicon-on-insulator wafers or deposited thin films [30, 31]. The fabrication is based on standard Si processing technology and performed on standard single crystalline silicon wafers, yielding a monolithic structure with excellent PC material quality and mechanical properties that far exceeds those of PCs made in deposited films (e.g. LPCVD silicon) or the device layer of the silicon-on-insulator wafers. The absence of material stress mismatch in the GOPHER PCs is particularly important, because it allows for fabrication of large-area devices that can be transferred to any flat substrate. The GOPHER process is also compatible with standard MEMS and CMOS processing, so photonic elements such as waveguides and filters can be integrated with ICs and other photonic devices [42]. Furthermore, the process facilitates fabrication of multi-layered structures with single photomask because the top layer can be used as a self-aligned mask for bottom layers [43]. Multi-layered structures have interesting and unique optical properties posing high potential in various applications including displacement sensing [37], temperature sensing [44], and tunable filters [34].

4.3.2 Fiber Tip Sensor Assembly

After the silicon PCs are fabricated on silicon wafers, we transfer and affix them to the facets of single mode optical fibers using different fixation techniques: point welding with a Focused Ion Beam (FIB) [10], template-assisted gluing with epoxy [44], and transfer-printing [23]. In the FIB method we utilize a FIB tool equipped with an Omniprobe micro-manipulator. First, we partially cut out the PC membrane with the ion-beam in a size large enough to completely cover the fiber core (Fig. 4.5a). Then we bring the Omniprobe needle tip in contact with the PC and weld the tip to the PC by selectively depositing a Platinum (Pt) patch onto the tip (Fig. 4.5b). The welding is done on the corner of the PC in order to prevent the Pt lump from affecting the PC optical property. Next, we lift the probe needle up to pull the PC apart by breaking the remaining connecting sections (Fig. 4.5c). The membrane is then transferred to a cleaved fiber facet and aligned to the fiber core such that light from the core interacts only with the silicon PC (Fig. 4.5d). Pt is deposited at the corners of the PC to bond it onto the fiber tip (Fig. 4.5e), and the probe tip is retracted after being disconnected from the PC by ion-milling. The assembled sensor is shown in Fig. 4.5f. The sensor has the transferred PC membrane size of $\sim$30 μm $\times$ 30 μm that covers the mode field size of the single mode input from the fiber (Corning SMF-28e). Larger membranes may be used as long as they fit within the 125 μm-diameter fiber facet.

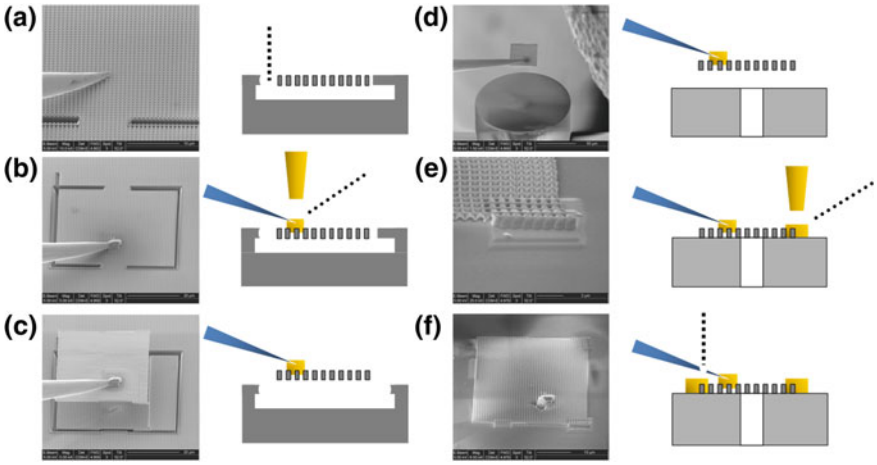

Fig. 4.5 Fiber sensor assembly using the FIB method: **a** a PC membrane is partially cut by ion-milling and the Omniprobe tip is brought in touch with the PC. **b** The probe tip is welded to the PC with Pt deposition. **c** The attached PC is pulled up and released from the substrate. **d** The PC is transferred onto to a fiber tip. **e** The PC is affixed to the fiber facet with Pt welding at its corners. **f** The probe tip is cut off by ion-milling. The *dotted line* represents the ion-beam

Even though the FIB method enables precise assembly of the PC membrane on the fiber tip, it is a serial process, which may limit the fast production of a large number of the sensors. The template-assisted epoxy bonding method is devised to accelerate the sensor fabrication with batch-production capability. We fabricate a silicon wafer template with a penetrating cylindrical hole whose diameter smaller than the fiber diameter (Fig. 4.6a). We apply an epoxy on the template (Fig. 4.6b) and apply suction through the hole, leaving the epoxy only on the boundary of the hole (Fig. 4.6c). The fiber facet is aligned to the hole and brought in contact with the template (Fig. 4.6d) so that the epoxy pattern is transferred onto the facet while keeping the fiber core clean from the epoxy (Fig. 4.6e). Next, the fiber is pressed on the PC membrane (Fig. 4.6f) and lifted up with the PC fixed to the facet after the epoxy hardens. The perforation in the PC membrane facilitates the separation and transfer process. This assembly method allows for economical batch production of the sensors with easy extension to harsh environment applications by replacing the epoxy with ceramic adhesives or glass glues [45]. However, this method may require more sophisticated modeling and analysis in the sensor characterization because a gap between the fiber tip and the PC due to the epoxy thickness and a tilt angle of the PC membrane with respect to the facet may influence the sensor responses. The transfer-printing technique can solve these issues by directly affixing two flat surfaces of separate devices [46]. A PC diaphragm fabricated on a silicon wafer can be picked up using a polymer microstamp, and then transferred and printed on an optical platform, e.g. a fiber facet. A high temperature annealing process is performed to form strong covalent

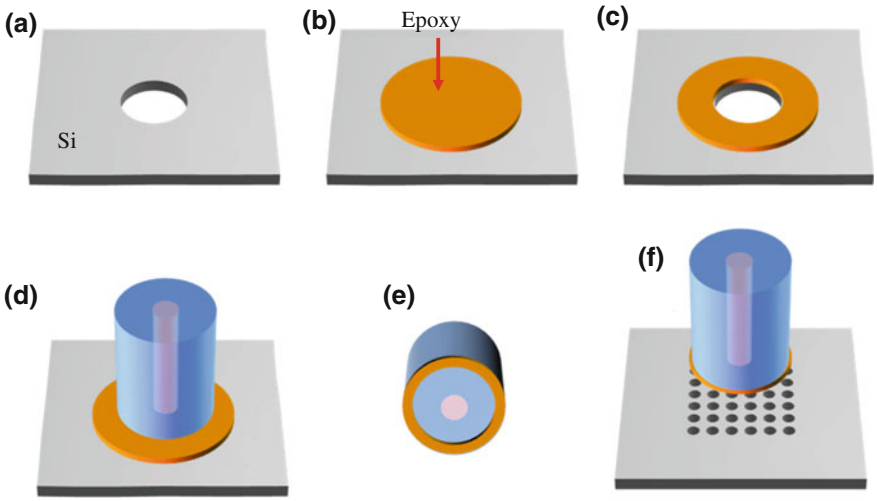

Fig. 4.6 Fiber sensor assembly using the template-assisted epoxy bonding: **a** a through-wafer hole is etched on a silicon wafer using Deep RIE. The hole diameter is smaller than the fiber diameter. **b** A small amount of an epoxy is applied around the hole. **c** Suction through the hole removes the epoxy on the hole and form a *ring pattern* on the hole edge. **d** A cleaved fiber is pressed on the template with fiber core aligned to the hole center. **e** The lifted fiber has the epoxy only on its facet boundary, which allows the guided light in the core to interact purely with the PC. **f** The fiber is pressed on the PC membrane and pulled away with the PC on it after the epoxy hardens

bonds at the interface, which allows for more robust sensor structure than the point-welding and the epoxy-gluing. However, the strict requirement of the flat surfaces on both devices may limit or complicate the design, geometry, and fabrication of the devices.

4.4 Fiber Tip Sensor Characterization

2-D PCs are very sensitive transducers whose reflection/transmission spectra are modulated in response to changes in their surrounding environment, and therefore our PC-mounted fiber sensors enable compact sensing on robust and reliable optical platforms. The incident optical field guided along the fiber is reflected back from the fiber-PC sensor, which is exposed to different measurands, and the modulation of the reflected signal, typically in a form of shifts in the PC reflection spectrum, is used to analyze changes in the internal states and surrounding medium of the PC sensor. In this section, we demonstrate refractive index and temperature sensing with our sensor, showing high sensitivity to both parameters. We also present high temperature performance that illustrates how its robust dielectric material composition makes it promising for applications in harsh environments.

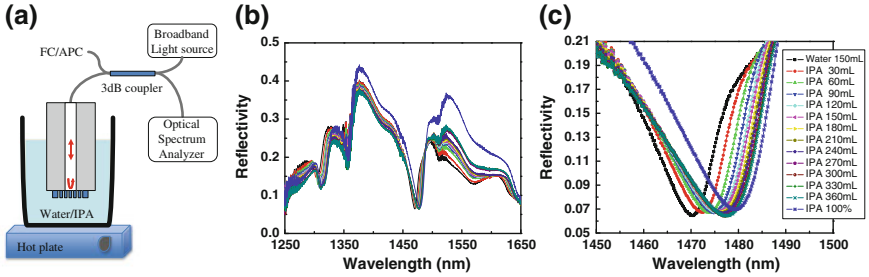

Fig. 4.7 **a** Experimental setup. **b** Measured reflection spectrum of a fiber sensor exposed to different DI water/IPA solution concentrations. **c** Zoomed-in view of the reflection minimum at about around 1475 nm wavelength. The reflection minimum is *red*-shifted as the IPA concentration increases. The graphs show that different parts of the spectra experiences different amounts of shift in response to changes in concentration

4.4.1 Sensitivity to Refractive Index

In order to examine the sensor response to refractive index variations, we immerse the sensor in a de-ionized(DI) water/isopropanol(IPA) solution with different concentrations at room temperature (Fig. 4.7a). The distal end of the fiber, onto which the sensor is integrated, is spliced to a 3 dB-couplers. The input to the 3-dB coupler is provided by a broadband light source (B&W TEK BWC-SLD for 1,250 ~ 1,650 nm). One output of the 3 dB coupler is connected to the sensor fiber, while the other output port is connected to an angled fiber connector to eliminate back reflections from that port. The back reflected optical field from the sensor is detected and spectrally resolved in an optical spectrum analyzer (Yokogawa AQ6370).

The reflection spectrum is measured at each concentration of the DI water/IPA solution. Figure 4.7b and c shows that the reflection spectra have a sharp and prominent minimum at about 1475 nm wavelength, and that the minimum shifts to higher wavelengths as the IPA concentration increases. The center wavelength shift of the reflectance minimum is plotted as a function of the effective refractive index of the solution in Fig. 4.8a. The measured sensitivity is ~213 nm/RIU (Refractive Index Unit), which is about 3 times larger than that of core-exposed FBG sensors (~71 nm/RIU) [6]. The measured spectra show that different features of the spectra experience different amounts of shift in response to changes in concentration. This is because the guided resonances of the PC sensor, which determines the spectra, have different dependence on the external refractive index variations. Therefore, each guided resonance excited at its resonant wavelength results in the dissimilar spectral shift across the wavelength range. The chosen spectral minimum represent close to the maximum sensitivity to refractive index of this specific sensor. In combination with a spectroscopic measurement system that has picometer resolution, the observed sensitivity leads to a refractive index resolution of $\Delta n \sim 5 \times 10^{-6}$.

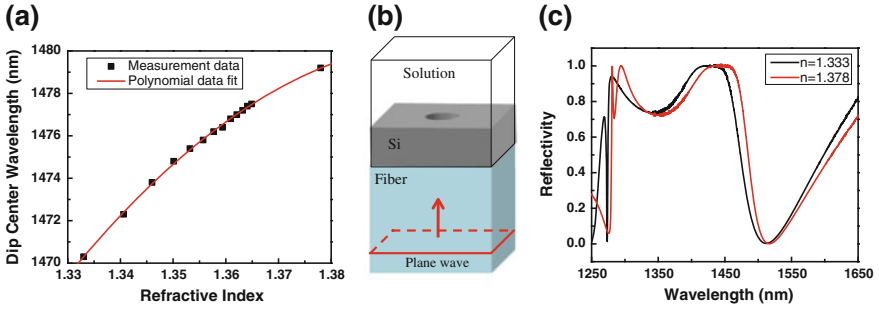

Fig. 4.8 **a** Plot of *center* wavelength shift of the reflection minimum around 1475 nm as a function of the effective refractive index of the solution being measured. **b** Unit cell model used in FDTD simulations of the sensor. The unit cell consists of a uniformly thick silicon slab with single cylindrical hole at its center and a glass substrate. **c** FDTD simulation results showing that the spectrum *red*-shifts as the refractive index increases. As in the measurements, the shift is not uniform over the wavelength range of the simulations

To understand and quantitatively describe the response of the sensor, we compare the experimental result to Finite Difference Time Domain (FDTD) simulations. The simplified simulation model consists of a top silicon layer with a cylindrical hole at its center and a bottom glass layer as shown in Fig. 4.8b. The hole and the region above the silicon layer are filled with a material corresponding to the effective index of the solution to be measured. The glass represents the fiber core, and a normally incident plane wave is used to model the incident optical field on the optical fiber. The sidewall boundaries are treated as periodic while the top and bottom of the simulation cell are terminated with perfectly matched layers. Although the model is a simplified version of the sensor, it predicts a shift of $\sim$222 nm for a refractive index change from 1.333 to 1.378 (Fig. 4.8c), closely matching the observed results.

4.4.2 Sensitivity to Temperature

For temperature measurements, the experimental setup in Fig. 4.7a is slightly modified. We immerse the same fiber sensor in DI water and control the water temperature using a hot plate. The reflection spectra (Fig. 4.9a) are measured while the water is cooled down from 80 °C. They exhibit the identical sharp reflection dip around 1472 nm wavelength shifting to lower wavelengths as the temperature decreases (Fig. 4.9b). The spectral shift of the minimum as a function of the temperature (Fig. 4.9c) shows that the temperature sensitivity of the sensor is $\sim$0.063 nm/°C, which is significantly better than that of FBG sensors [9].

We also compare the temperature results to FDTD simulations. In these simulations, we only consider the thermo-optic effect of the silicon photonic crystal and water, i.e. the temperature dependent refractive index change [47, 48], and we

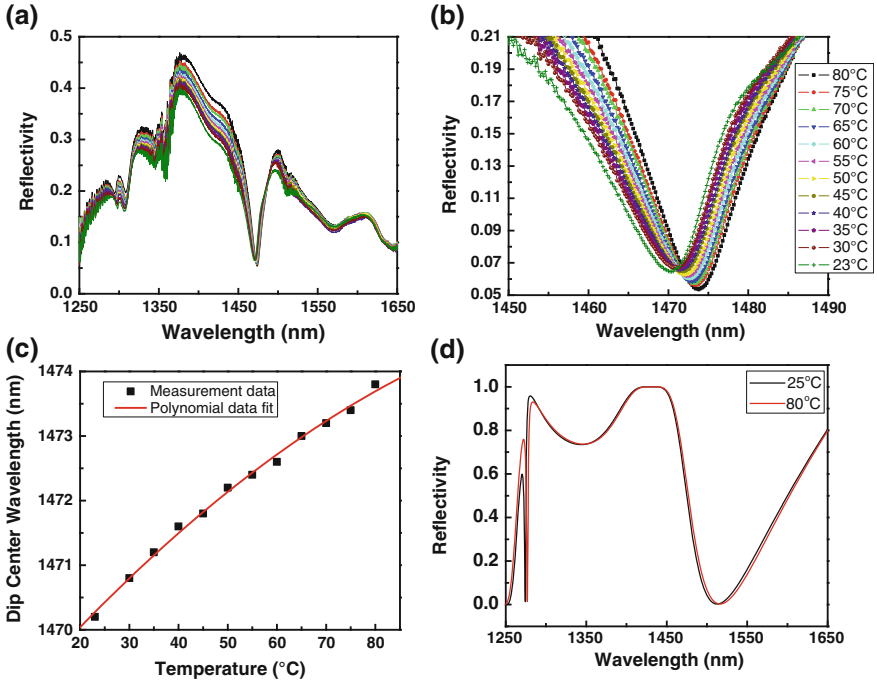

Fig. 4.9 **a** Measured reflection spectra of the fiber sensor (the same sensor as in Fig. 4.7) at different temperatures. **b** Zoomed view of the reflection minimum at about 1472 nm wavelength. **c** Plot of the reflection minimum center wavelength as a function of temperature. **d** FDTD simulation result showing a *red*-shift of 3.6 nm for temperature increase from 25 to 80 °C

ignore dimensional changes. Using this simplified model, we predict a shift of ~3.6 nm from 80 °C to room temperature (Fig. 4.9d), which agrees well with the measured shift of ~3.4 nm. Our model reveals that the refractive indices of the PC and a surrounding measurand are the dominant factors determining the thermal response of the sensor, while other effects such as thermal expansion of the PC and refractive index changes of the fiber are less significant. The fiber is composed of glass whose thermo-optic coefficient is an-order of magnitude smaller than that of silicon [49], which explains its relative insignificance.

4.4.3 Simultaneous Detection of Refractive Index and Temperature

The high sensitivity of our sensor to both refractive index and temperature of the environment means that its spectral response is determined by the combined effects of the two. Therefore, it is very important to unambiguously distinguish between them when we measure the sensor output. A sensor with single characteristic

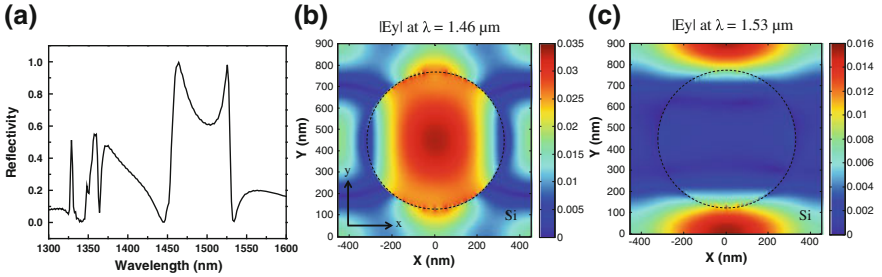

Fig. 4.10 **a** FDTD simulated reflection spectrum of a 2-D PC (periodicity = 900 nm, hole diameter = 640 nm, and thickness = 550 nm) on a fiber using the model in Fig. 4.8b. The surrounding medium is IPA at 25 °C. **b** Electric field distribution($|E_y|$) in the PC symmetry plane at $\lambda = 1.39$ μm. **c** Electric field distribution($|E_y|$) in the PC symmetry plane at $\lambda = 1.55$ μm. The electric field is calculated with the FDTD simulation. The hole boundary is shown as *dotted line*

resonance does not support this capability because both quantities affect its output. However, 2-D PCs have multiple guided resonances at different wavelengths, and each resonance has a different field configuration inside and outside the PC. Accordingly they are expected to respond differently to internal and external changes in PC; external refractive index variation in the vicinity of the PC body interacts with the outside field whereas the inside field is sensitive to internal refractive index variations, which are mainly due to temperature change.

To clarify this effect, a 2-D PC (periodicity = 900 nm, hole diameter = 640 nm, and thickness = 550 nm) on a fiber immersed in an IPA is simulated using the FDTD simulation model presented in Fig. 4.8b. The simulated reflection spectrum is shown in Fig. 4.10a. For a resonant peak at $\lambda = 1.46$ μm the PC has a strong electric field inside the hole and weak field inside the silicon (Fig. 4.10b), whereas for a resonant dip at $\lambda = 1.53$ μm the field is very weak inside the hole and strong in the silicon (Fig. 4.10c). As a result, the mode at $\lambda = 1.53$ μm is selectively sensitive to temperature changes which affect the refractive index of silicon PC body. On the other hand, the mode at $\lambda = 1.46$ μm is sensitive to changes in the refractive index of a surrounding measurand. By examining the independent behaviors of such two modes with selective sensitivity to either temperature or refractive index, we can simultaneously determine two parameters of a medium to be measured. An experimental demonstration of this capability is described in [10]. In comparison, the previous fiber sensor shows maximum refractive index and temperature sensitivity at the same reflection dip wavelength because the corresponding mode is sensitive to both parameters. Therefore, this mode is not suitable for discrimination of two quantities.

4.4.4 High Temperature Measurement

The combination of high sensitivity to refractive index and temperature with its compact construction using robust, high temperature dielectric materials (silicon

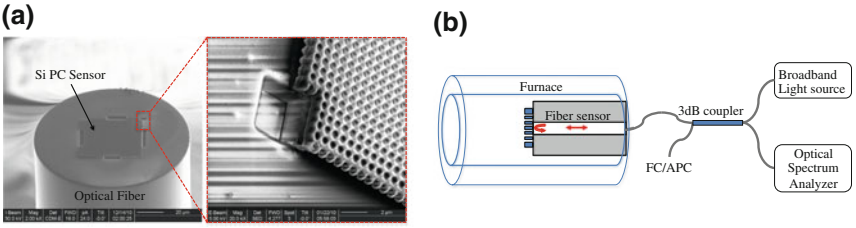

Fig. 4.11 **a** Fiber sensor for high temperature measurement and *zoomed view* of Si-welding bonding at the PC-fiber interface. **b** Experimental setup for high temperature measurement

for the PCs and silicon oxide for the fibers), gives our sensors the potential for operation in harsh environments. In this section, we explore its thermal response and stability in high temperatures up to 900 °C. For this purpose, we integrate our PC sensors onto optical fiber using Si-welding bonding as shown in Fig. 4.11a. This method avoids FIB deposited Pt, which contains organic material from its metal-organic precursor and may decompose at high temperatures. Instead, we mill the corners of the PC membrane with an ion beam, which leads to sputtering and re-deposition of Si and oxide at the PC-fiber interface, yielding strong bonds, which further enhance the sensor's stability at high temperature by avoiding thermal stress mismatch with Pt.

4.4.4.1 Experimental Setup

The high temperature experimental setup is similar to the previous setup except that the sensor is positioned inside a quartz furnace as shown in Fig. 4.11b. We cycle the temperature over 100–700 °C five times and measure the sensor reflection spectra at every 100 °C change. Each cycle consists of heating and cooling over the temperature range. These repeated measurements are designed to check the stability of our sensors at high temperature. We also increase the temperature above 700 °C and perform heating and cooling cycles in the 700–900 °C temperature range with spectral measurements at 50 °C intervals. This higher temperature range is expected to exceed the sensor's stable operation regime. The anomalous behavior of our sensors in this temperature range will be analyzed in detail in the Sect. 4.4.4.2. The upper limit of 900 °C is chosen because the reliability of optical fibers greatly decreases beyond this temperature due to thermal diffusion of the fiber core dopants and glass devitrification [2].

4.4.4.2 Measurement Analysis and Simulation

For measurements in the 100–700 °C range, we observe that a narrow reflection dip shifts from 1500 to 1580 nm wavelength with the same trend as in previous temperature measurements; the spectra red-shifts when the temperature increases

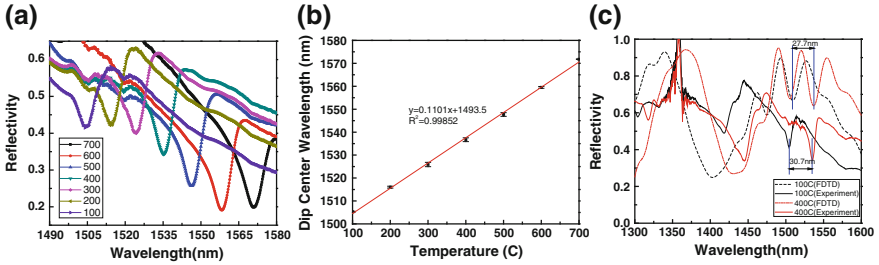

Fig. 4.12 **a** Reflection spectra measured during the fifth cooling cycle (700 to 100 °C). **b** Dip center wavelength with respect to temperature during 100–700 °C temperature cycles. The slope or sensitivity of the sensor is 0.11 nm/°C. **c** Comparison of FDTD simulation and experimental data: a simulated 27.7 nm maximum shift agrees well with an experimental 30.7 nm shift for a temperature change from 100 to 400 °C

while it blue shifts when the temperature decreases. Figure 4.12a clearly shows the blue-shift during the fifth cooling cycle. The center wavelengths of the reflection minimum measured during five cycles are plotted as a function of temperature in Fig. 4.12b. They coincide with each other with a linear sensitivity slope of 0.11 nm/°C. This demonstrates not only stable and repeatable sensor operation in this temperature range, but also the very high temperature sensitivity of the sensor compared to that of high-temperature FBG sensors ($\sim$0.01 nm/°C) [9].

We also run FDTD simulations to clarify the physics of the sensors at high temperature. We extend the simulation model in Fig. 4.8b by incorporating the characteristics of the optical fields on single-mode fibers into the model. In practical single mode fibers, the guided mode profile can be approximated as a Gaussian shape propagating within the core. Therefore, we build a large simulation cell of finite silicon PC hole arrays sitting on a glass cube with a cylindrical core of slightly higher refractive index at the center. Perfectly matched layers are applied to all boundaries, and the input is a Gaussian beam with the mode size matching the mode field diameter of a standard single mode fiber (SMF) at 1550 nm wavelength. The 2-D PC has the following dimensions: periodicity = 850 nm, hole diameter = 700 nm, and thickness = 520 nm. GOPHER-generated 120 nm-high scallops are added to the bottom of the PC.

Again we are only considering temperature-induced changes to the materials of the sensor due to the thermo-optic effect of silicon and glass [47, 49], while we ignore dimensional changes. The simulation results for 100 and 400 °C are presented together with experimental data in Fig. 4.12c. Although the simulated curves do not match exactly, the simulated shift of 27.7 nm closely predicts the experimental shift of 30.7 nm. We expect that the discrepancy is due to the simplifications we make in modeling of the PC-fiber system (e.g. spherical GOPHER undercut, fixed PC dimension, and wavelength-independent input modal size). The relatively close match of experimental and modeling results indicates that the thermo-optic effect of the sensor materials is the main factor determining the sensor's thermal response. Since silicon ($\sim 10^{-4}$ K^{-1}) has an order of magnitude higher thermo-optic

coefficient than glass ($\sim 10^{-5}$ K^{-1}) [47, 49], the silicon PC has the largest impact on the temperature sensitivity. The observation that our sensor has 10x higher sensitivity than FBGs can be explained from this material point of view; FBG relies on the thermo-optic effect of glass, the core material of the optical fiber. If higher sensitivity is required for an application, other semiconductor materials with larger thermo-optic coefficient, such as GaAs ($\sim 1.25 \times 10^{-4}$ K^{-1}) and Ge ($\sim 3 \times 10^{-4}$ K^{-1}) can be used for PC sensor fabrication [50, 51]. However, their lower melting points may limit the maximum operation temperature of the sensor.

We test the sensor's operation limit by raising the temperature above 700 °C and cycling heating and cooling over 700–900 °C three times. The dip center wavelengths at every 50 °C interval are plotted as a function of temperature in Fig. 4.13a. Two distinct phenomena, which are different from the previous 700–900 °C results, are observed. First, as the temperature approaches 900 °C in one heating cycle, the dip shift gradually deviates from the previous linear trend towards a decreased slope and consequently lower sensitivity. Second, a permanent spectral drift is observed after each cycle and the amount of the drift per cycle decreases as the cycles repeat.

We first discuss how the sensitivity is reduced above 700 °C. The refractive index of silicon is reported to increase linearly up to 750 °C [52], and this thermo-optic effect of silicon plays a significant role in the sensor's spectral behavior as described previously. Therefore, the lower sensitivity indicates that the effective thermo-optic coefficient of the silicon PC decreases as the temperature is heated to 900 °C. At such high temperatures, silicon thermal oxidation starts and the in situ grown oxide film exerts stress on the silicon PC surface, which compensates for the increase in its refractive index [53]. The net result is smaller thermo-optic effect in the PC and hence smaller dip shifts. We compare the measured dip shift to a simulated value to confirm the effect of oxidation-induced stress on the sensor. The sensor stays above 700 °C for more than 40 min per cycle in our experiment, and we measure the thermal oxide film thickness on a PC sample under one temperature cycle to be 18.2 nm using an ellipsometer (J.A. Woollam M2000 Spectroscopic Ellipsometer) as shown in Fig. 4.13b. The corresponding average oxide film stress at 846 °C is about 300 MPa [54], and we analytically calculate the silicon surface stress to be $\sim$1GPa under the assumption of the ideal bending stress distribution over the cross-section of a composite beam. This leads to stress-induced silicon refractive index decrease of 0.01 [53]. When this effect is considered in FDTD simulations, a 7.34 nm blue-shift is predicted (Fig. 4.13c). This value closely matches the measured offset of 4.5–10 nm compared to the values extrapolated from the 100–700 °C data. In addition to the decreased thermo-optic effect, the PC dimensions slightly changes as thermal oxidation consumes silicon; the PC becomes thinner and its hole diameter becomes larger. Also, the grown oxide layer conformally covers the PC surface. When all these effects (dimension change, oxide coating, stress-induced refractive index change) are taken into account in the FDTD simulations, a 30.6-nm dip shift is predicted as shown in Fig. 4.13d. This is also consistent with the total measured drift after three temperature cycles. The good agreement between the oxidation model and the

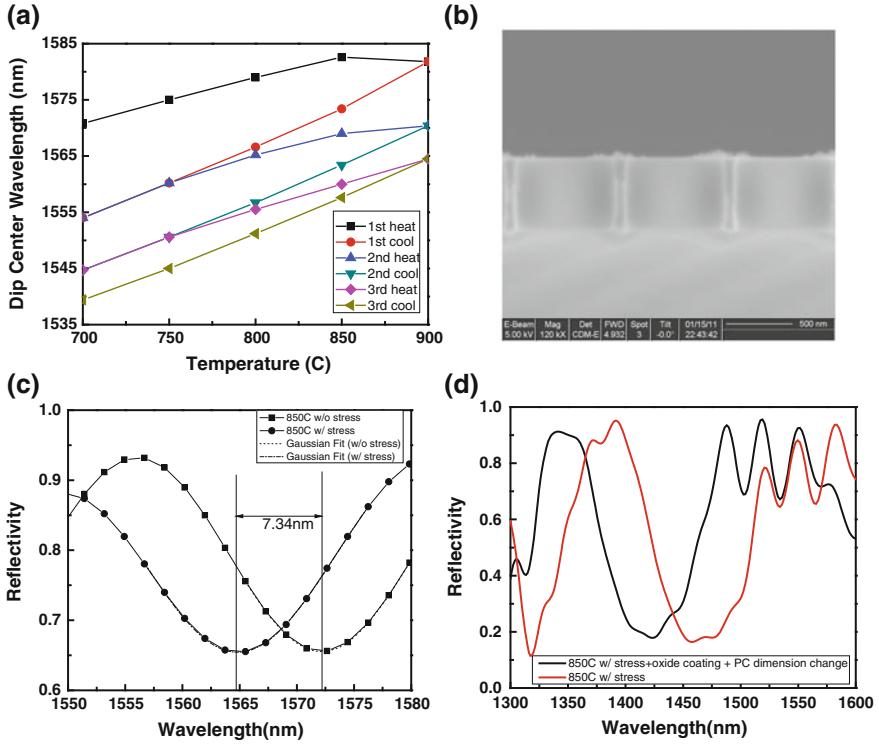

Fig. 4.13 **a** Maximum spectral wavelength shift as a function of temperature during three cycles over 700 ~ 900 °C. The slope of the shift decreases at the *upper end* of the heating cycle and a permanent shift occurs after each cycle **b** SEM image of the PC membrane crosssection where a 18.2 nm-thick oxide layer is grown during one temperature cycle (700 ~ 900 °C) **c** FDTD simulation with and without the thermal oxidation-induced refractive index decrease at 850 °C. The oxidation model predicts the dip shift of 7.34 nm, matching the experimental result above 700 °C. **d** FDTD simulation with and without growth of conformal oxide and the corresponding PC dimensional change. The shift of 30.6 nm closely matches the measurement after three cycles

experimental results is a strong indication that in situ oxide stress is a big factor for the sensitivity reduction above 700 °C.

The second observed anomalous behavior is the permanent drift of the resonance dip after each cycle. During the cooling process, the dip center wavelength shift is linear with a slightly higher sensitivity of 0.12 ~ 0.13 nm/°C. This is likely caused by the fact that the refractive index modulation due to existing surface stress constructively adds to the original thermo-optic effect. The difference in the slope during heating and cooling stages results in the observed drift. Moreover, plastic deformation of the silicon structure may also be a factor because the silicon yield strength decreases at high temperature and is lower than the calculated stress at 700 °C or above [55]. The thermal oxidation and the plastic deformation are irreversible, and therefore lead to a permanent spectral shift

However, the amount of shift decreases after each cycle because of the slow-down of the oxidation process with thicker oxide coverage and relaxation of the oxide film and the silicon.

In summary, our PC fiber tip sensor can reliably operate up to 700 °C with a high sensitivity of 0.11 nm/°C, but thermal oxidation of the silicon PC brings about lower sensitivity and permanent shifts beyond 700 °C. The stable temperature range of the sensor can be extended above 700 °C by applying a conformal oxidation barrier film on the silicon PC or using more robust materials, e.g. silicon carbide (SiC) for PCs [56].

4.5 Conclusion

Photonic Crystal fiber facet sensors are highly sensitive and well suited to operation in challenging environments. The monolithic silicon PCs are fabricated using the GOPHER process, which is based on standard Si processing and standard Si wafers. The batch fabricated PCs are integrated onto fiber facets using one of several micro-assembly techniques optimized for different applications; FIB welding yields robust interfaces, while template-assisted adhesive bonding or transfer-printing are more cost effective. The fiber-facet design enables compact fiber sensors that are mechanically, thermally, and chemically robust in spite of the fact that they are comprised of different materials (glass and Si). The ability to combine different materials without compromising robustness enables the design of high sensitive refractive index and temperature sensors. These sensors are especially promising for harsh environment, such as oil wells, gas turbines, automotive engines, geothermal instruments, and aircraft propulsion systems, where other sensors fail due to corrosive chemicals and high temperature/pressure. Moreover, 2-D PC slab on fiber facet sensor technology facilitates optimization and extension of the sensor performance through several types of modifications of the PCs: the use of different materials (e.g. higher thermo-optic coefficient, higher melting point), surface functionalization or passivation, and multi-layered PC structures.

References

1. E. Udd, Overview of fiber optic sensors. Rev. Sci. Instrum. **66**, 4015–4030 (1995)
2. A. Wang, Y. Zhu, G. Pickrell, Optical fiber high-temperature sensors. Opt. Photon. News **20**, 26–31 (2009)
3. A.D. Kersey et al., Fiber grating sensors. JLT **15**(8), 1442–1463 (1997)
4. G. Meltz, W.W. Morey, W.H. Glenn, Formation of Bragg gratings in optical fibers by transverse holographic method. Opt. Lett. **14**, 823–825 (1989)
5. V. Bhatia, A.M. Vengsarkar, Optical fiber long-period grating sensors. Opt. Letters **21**(9), 692–694 (1996)
6. W. Liang, Y. Huang, Y. Xu, R.K. Lee, A. Yariv, Highly sensitive fiber Bragg grating refractive index sensors. Appl. Phys. Lett. **86**, 151122-1–151122-3 (2005)

7. S. James, R. Tatam, Optical fibre long-period grating sensors: characteristics and application. Meas. Sci. Technol. **14**, R49 (2003)
8. T. Ergodan, V. Mizrahi, P.J. Lemaire, D. Monroe, Decay of ultraviolet-induced fiber Bragg gratings. J. Appl. Phys. **76**, 73–80 (1994)
9. T.L. Lowder et al., High-temperature sensing using surface relief fiber Bragg gratings. IEEE Photonics Technol. Lett. **17**(9), 1926–1928 (2005)
10. I. Jung, B. Park, J. Provine, R. Howe, O. Solgaard, Highly sensitive monolithic silicon photonic crystal fiber tip sensor for simultaneous measurement of refractive index and temperature. J. Lightwave Technol. **29**, 1367–1374 (2011)
11. B. Park, J. Provine, I. Jung, R. Howe, O. Solgaard, Photonic crystal fiber tip sensor for high-temperature measurement. IEEE Sens. J. **11**(11), 2643–2648 (2011)
12. S.-K. Eah, H.M. Jaeger, N.F. Scherer, G.P. Wiederrecht, X.-M. Lin, Plasmon scattering from a single gold nanoparticle collected through an optical fiber. Appl. Phys. Lett. **86**, 031902-1–031902-3 (2005)
13. O.C. Akkaya, M. Digonnet, G.S. Kino, O. Solgaard, Modeling and demonstration of thermally stable high-sensitivity reproducible acoustic sensors. J. Microelectromech. Syst. **21**(6), 1347–1356 (2012)
14. E. Yablonovitch, Photonic band-gap structures. J. Opt. Soc. Am. B **10**(2), 283–295 (1993)
15. H. Kosaka, T. Kawashima, A. Tomita, M. Notomi, T. Tamamura, T. Sato, S. Kawakami, Superprism phenomena in photonic crystals. Phys. Rev. B **58**(16), R10096–R10099 (1998)
16. C. Luo, S.G. Johnson, J.D. Joannopoulos, J.B. Pendry, All-angle negative refraction without negative effective index. Phys. Rev. B **65**, 201104(R) (2002)
17. S. Fan, J.D. Joannopoulos, Analysis of guided resonances in photonic crystal slabs. Phys. Rev. B **65**, 235112 (2002)
18. S. Lin, E. Chow, V. Hietala, P.R. Villeneuve, J.D. Joannopoulos, Experimental demonstration of guiding and bending of electromagnetic waves in a photonic crystal. Science **282**, 274–276 (1998)
19. B. Ellis, M.A. Mayer, G. Shambat, T. Sarmiento, J. Harris, E. Haller, J. Vučković, Ultralow-threshold electrically pumped quantum-dot photonic-crystal nanocavity laser. Nat. Photonics **5**, 297–300 (2011)
20. M. Lee, P.M. Fauchet, Two-dimensional silicon photonic crystal based biosensing platform for protein detection. Opt. Express **15**(8), 4530–4535 (2007)
21. I.W. Jung, S.B. Mallick, O. Solgaard, A large-area high-reflectivity broadband monolithic single-crystal silicon photonic crystal mirror MEMS scanner with low dependence on incident angle and polarization. J. Sel. Top. Quan. Elect. **15**, 1447–1454 (2009)
22. J.C. Knight, T.A. Birks, P.St.J. Russell, D.M. Atkin, Pure silica single mode fiber with hexagonal photonic crystal cladding. Presented at the conference on optical fiber communication (OFC), San Jose, CA, Mar 1996, Postdeadline paper PD3
23. J. Jeong, B. Park, H. Keum, S. Kim, J. Rogers, O. Solgaard, Two-axis MEMS scanner with transfer-printed high-reflectivity, broadband monolithic silicon photonic crystal mirrors. Opt. Express **21**, 13800–13809 (2013)
24. T.G. Euser, A.J. Molenaar, J.G. Fleming, B. Gralak, A. Polman, W.L. Vos, All-optical octave-broad ultrafast switching of Si woodpile photonic band gap crystals. Phys. Rev. B **77**, 115214-1-6 (2008)
25. K.M. Ho, C.T. Chan, C.M. Soukoulis, Existence of a photonic gap in periodic dielectric structures. Phys. Rev. Lett. **65**, 3152 (1990)
26. M. Deubel, M. Wegener, S. Linden, G. von Freymann, S. John, 3D-2D-3D photonic crystal heterostructures fabricated by direct laser writing. Opt. Lett. **31**, 805–807 (2006)
27. R.C. Schroden, M. Al-Daous, C.F. Blanford, A. Stein, Optical properties of inverse opal photonic crystals. Chem. Mater. **14**(8), 3305–3315 (2002)
28. W. Suh, Photonic crystal slabs: theory and applications. Ph.D. dissertation, Stanford Univ., Stanford, CA (2006)

29. W. Suh, M. F. Yanik, O. Solgaard, S.-H. Fan, Displacement-sensitive photonic crystal structures based on guided resonance in photonic crystal slabs. Appl. Phys. Lett. **82**(13), 1999–2001 (2003)
30. K.B. Crozier, V. Lousse, O. Kilic, S. Kim,W. Suh, S. Fan, O. Solgaard, Air-bridged photonic crystal slabs at visible and near-infrared wave lengths. Phys. Rev. B (Condens. Matter Mater. Phys.) **73**(11), 115126-1-14 (2006)
31. V. Lousse, W. Suh, O. Kilic, S. Kim, O. Solgaard, S. Fan, Angular and polarization properties of a photonic crystal slab mirror. Opt. Express **12**, 1575–1582 (2004)
32. O. Kilic, S. Kim, W. Suh, Y.-A. Peter, A.S. Sudbø, M.F. Yanik, S. Fan, O. Solgaard, Photonic crystal slabs demonstrating strong broadband suppression of transmission in the presence of disorders. Opt. Lett. **29**, 2782–2784 (2004)
33. O. Kilic, S. Fan, O. Solgaard, Analysis of guided-resonance based polarization beam splitting in photonic crystal slabs. J. Opt. Soc. Am. A **25**(11), 2680–2692 (2008)
34. W. Suh, S. Fan, Mechanically switchable photonic crystal filter with either all pass transmission or flat-top reflection characteristics. Opt. Lett. **28**, 1763–1765 (2003)
35. O. Kilic, M. Digonnet, G. Kino, O. Solgaard, External fibre Fabry-Perot acoustic sensor based on a photonic-crystal mirror. IOP Publishing Meas. Sci. Technol. **18**, 3049–3054 (2007)
36. X. Wu, O. Solgaard, Short-cavity multimode fiber-tip Fabry-Perot sensors. Opt. Express **21**, 14487–14499 (2013)
37. W. Suh, O. Solgaard, S. Fan, Displacement sensing using evanescent tunneling between guided resonances in photonic crystal slabs. J. Appl. Phys. **98**, article 033102 (2005)
38. J.O. Grepstad, P. Kaspar, O. Solgaard, I.-R. Johansen, A.S. Sudbø, Photonic-crystal membranes for optical detection of single nano-particles, designed for biosensor application. Opt. Express **20**, 7954–7965 (2012)
39. M. El Beheiry, V. Liu, S. Fan, O. Levi, Sensitivity enhancement in photonic crystal slab biosensors. Opt. Express **18**, 22702–22714 (2010)
40. D. Threm, Y. Nazirizadeh, M. Gerken, Photonic crystal biosensors towards on-chip integration. J. Biophotonics **5**(8–9), 601–616 (2012)
41. S. Hadzialic, S. Kim, A.S. Sudbo, O. Solgaard, Two-dimensional photonic crystals fabricated in monolithic single-crystal silicon. PTL **22**(2), 67–69 (2010)
42. C.-M. Chang, O. Solgaard, Monolithic silicon waveguides in standard silicon. IEEE Micro **33**(1), 32–40 (2013)
43. S.B. Mallick, I.-W. Jung, A.M. Meisner, J. Provine, R.T. Howe, O. Solgaard, Multilayered monolithic silicon photonic crystals. IEEE Photonics Technol. Lett. **23**(11), 730–732 (2011)
44. B. Park, I. Jung, J Provine, R.T. Howe, O. Solgaard, Double-layer silicon photonic crystal fiber tip temperature sensor, in *2012 IEEE Photonics Conference (IPC)*, pp. 550, 551, 23–27 Sept 2012
45. S. Sinha, K. Urbanek, A. Krzywicki, R. Byer, Investigation of the suitability of silicate bonding for facet termination in active fiber devices. Opt. Express **15**, 13003–13022 (2007)
46. S. Kim, J. Wu, A. Carlson, S.H. Jin, A. Kovalsky, P. Glass, Z. Liu, N. Ahmed, S.L. Elgan, W. Chen, P.M. Ferreira, M. Sitti, Y. Huang, J.A. Rogers, Microstructured elastomeric surfaces with reversible adhesion and examples of their use in deterministic assembly by transfer printing. Proc. Nat. Acad. Sci. **107**, 17095 (2010)
47. H.H. Li, Refractive index of silicon and germanium and its wavelength and temperature derivatives. J. Phys. Chem. Ref. Data **9**, 561 (1980)
48. A.N. Bashkatov, E.A. Genina, Water refractive index in dependence on temperature and wavelength: a simple approximation. Proc. SPIE **5068**, 393–395 (2003)
49. C.Z. Tan, J. Arndt, Temperature dependence of refractive index of glassy SiO_2 in the infrared wavelength range. J. Phys. Chem. Solids **61**, 1315–1320 (2000)
50. B.J. Frey, D.B. Leviton, T.J. Madison, Temperature-dependent refractive index of silicon and germanium. Proc. SPIE **6273**, 62732J (2006)

51. F.G. Della Corte, G. Cocorullo, M. Iodice, I. Rendina, Temperature dependence of the thermo-optic coefficient of InP, GaAs, and SiC from room temperature to 600 K at the wavelength of 1.5 μm. Appl. Phys. Lett. **77**(11), 1614–1616 (2000)
52. G.E. Jellison Jr, H.H. Burke, The temperature dependence of the refractive index of silicon at elevated temperatures at severed laser wavelengths. J. Appl. Phys. **60**, 841 (1986)
53. S.M. Weiss, M. Molinari, P.M. Fauchet, Temperature stability for silicon-based photonic band-gap structures. Appl. Phys. Lett. **83**, 1980 (2003)
54. C. Yu, P.A. Flinn, J.C. Bravman, In situ stress measurements during dry oxidation of silicon. Mat. Res. Soc. Symp. Proc. **473**, 323–328 (1997)
55. J. Rabier, J.L. Demenet, Low temperature, high stress plastic deformation of semiconductors: the silicon case. Pysica Status Solidi (B) **222**(1), 63–74 (2000)
56. M. Mehregany, C.A. Zorman, N. Rajan, C. Wu, Silicon carbide MEMS for harsh environments. Proc. IEEE **86**(8), 1594–1609 (1998)